4D printing of Metal-Reinforced double network granular hydrogels

Matteo Hirsch [a], Livia D'Onofrio [a], Qinghua Guan [b], Josie Hughes [b], Esther Amstad [a],[*]

[a] Soft Materials Laboratory, Institute of Materials, École Polytechnique Fédérale de Lausanne, 1015 Lausanne, Switzerland
[b] CREATE Lab, Institute of Mechanical Engineering, École Polytechnique Fédérale de Lausanne, 1015 Lausanne, Switzerland

A B S T R A C T

Recent developments in soft actuation demand for resilient, responsive materials with locally varying compositions that are sufficiently stiff to exhibit significant actuation forces. Hydrogels are inherently responsive to certain stimuli. Yet, they typically suffer from a stiffness-toughness compromise such that those that are soft and show adequate flexibility display limited actuation forces. This compromise can be partially addressed if hydrogels are formulated as double networks. However, their involved processing prevents controlled variations in the local composition. The composition of hydrogels can be varied down to the 100 μm length scale through 3D printing. A wide range of hydrogels can be 3D printed if formulated as microparticles. Yet, the resulting granular hydrogels are soft. They can be reinforced with a percolating hydrogel network, resulting in double network granular hydrogels (DNGHs) that, however, are rather brittle. Here, we introduce 3D printable metal-reinforced DNGHs (mrDNGHs) that combine three seemingly contradictory traits: stiffness, toughness, and processability. Our mrDNGHs can bear loads up to 3 MPa while displaying a fracture energy up to 12 MJ·m^{-3}, a value exceeding that of any of the previously 3D printed hydrogels at least 20-fold. We leverage the different degrees of swelling of the mrDNGHs to 3D print shape morphing structures.

1. Introduction

Nature has been a tremendous source of inspiration for the design of functional materials [1]. Excellent work performed in this area offers a good understanding of the composition-structure–function relationship of a wide variety of natural materials [2,3]. For instance, the analysis of the composition of certain soft biological tissues revealed that nature achieves self-healing and dynamic stress response through non-covalent interactions [4–6]. One remarkable example is the mussel byssus, an acellular soft load-bearing tissue that allows the organism to strongly anchor to the rocks to even withstand the shear of impacting waves that exert shear stresses up to 40 MPa [3]. Inspired by nature, soft synthetic materials have been mechanically reinforced through non-covalent reversible interactions [7–9], such as host–guest [10,11] or hydrophobic interactions [12,13], metal coordination [14–17], and covalent reversible crosslinkers [18,19]. Despite the substantial improvement in mechanics of synthetic soft materials, nature's fine interplay between structure and composition remains unmatched. A fundamental reason behind this mismatch in mechanical properties is that manmade constructs typically possess homogeneous structures and compositions compared to the well-defined hierarchical structures and abruptly changing compositions of their natural counterparts [20–22]. Recently, several strategies have been implemented to control the structure of soft synthetic materials at different length scales [9,23–25], including directed self-assembly [26–29], phase separation [30–34], microfluidics

[35,36], and 3D printing [37–41]. However, these techniques offer a limited control over the spatial resolution. To increase the level of control over the microstructure in manmade soft materials and widen the range of soft materials that can be 3D printed, a novel class of 3D printable materials, jammed microgels, has been introduced [36,42–47]. Microgels are micrometer-sized hydrogel particles that undergo jamming when concentrated above a critical volume fraction [24,48]. Yet, the resulting granular hydrogels are soft due to weak inter-particle connections. This shortcoming can be overcome by reinforcing granular hydrogels with a percolating hydrogel network that interpenetrates and covalently crosslinks them [18,49]. However, the resulting double network granular hydrogels display a limited strain at break, with cracks that preferentially propagate along the grain boundaries [50,51].

Here, we introduce 3D printable metal-coordinated DNGHs whose stiffness exceeds that of any previously reported 3D printed hydrogel 12-fold and whose fracture energy is more than 20-fold higher than that of any 3D printed hydrogel reported thus far. This is achieved by forming microfragments from poly(acrylic acid) (PAA) that can be reinforced with a wide range of cations. We demonstrate that the stiffness of DNGHs made by covalently crosslinking these microfragments with a percolating polyacrylamide (PAM) hydrogel is 0.12 MPa, whereas their work of fracture is 0.02 MJ·m^{-3}. The work of fracture of DNGHs increases by more than two orders of magnitudes, up to 12 MJ·m^{-3}, if the percolating network is ionically reinforced, as demonstrated on DNGHs

composed of PAM microfragments that are connected through a metal-reinforced PAA network. We demonstrate the potential of these materials in soft actuation by 3D printing shape morphing structures.

2. Results and discussion

To ionically reinforce granular double network hydrogels, we form one of the hydrogel networks from poly(acrylic acid) (PAA), a polyelectrolyte that can be reinforced with different ions possessing a valency of at least two [15,52,53]. To render PAA 3D printable, we formulate it as granules. Granules can be fabricated from emulsion drop templates produced through batch emulsification [49], or if a tighter size-control is warranted through microfluidics [54–57]. These water-in-oil emulsions must be stabilized with surfactants that, together with the oil, must be removed through several washing steps after the microgels have been produced, thereby limiting the throughput of this technique and increasing the production costs [44]. Microgels can also be made through precipitation polymerization [58] or spray emulsification [59], yet with more stringent requirements in terms of material selection and precursor viscosity. A way to circumvent these shortcomings is to mechanically fragment bulk hydrogels [44,60–62] for example using blenders [63], sieves [61], or cryomilling [62]. Cryomilling is particularly attractive because it enables breaking any material whose T_g is above the temperature of liquid nitrogen (-196 °C) into microfragments at high throughputs, albeit at the expense of shape control [62]. Taking advantage of the high throughput and versatility in terms of material choice, we cryo-mill PAA into microfragments that are non-spherical and display an equivalent diameter (d^*), calculated as the average of the two diagonals of the particle, of 45 μm, independent of the acrylic acid monomer content, as shown in Fig. S1.

To firmly connect adjacent microfragments after they have been 3D printed, we soak them in an aqueous solution containing acrylamide before they are jammed to enable their 3D printing, as schematically shown in Fig. 1a. After the ink has been 3D printed, we connect microfragments by exposing the printed structure to UV light. Thereby, we initiate the polymerization of the acrylamides contained in the

microfragments to form a percolating network that interpenetrates and crosslinks them, resulting in a DNGH, as shown in Fig. 1b. The granular nature of DNGHs allows for the selective reinforcement of the certain grains, thus enabling the fabrication of heterogeneously reinforced DNGHs, as schematically shown in Fig. 1c. The ability to spatially vary the DNGH composition through 3D printing opens up new possibilities to 3D print load-bearing, actuatable hydrogels, as schematically shown in Fig. 1d.

DNGHs are composed of densely packed microfragments. Hence, their microstructure is determined by the size, size distribution, morphology and packing density of the microfragments. The average dimensions of microfragments and their distribution depend on the cryomilling parameters, including the milling frequency, size of the milling spheres, and the number the of milling cycles [62]. For printing applications, we aim at obtaining fragments that are smaller than 100 μm to avoid clogging of the nozzle while maintaining a high throughput production of the microfragments. To test the influence of the number of milling cycles the hydrogel has been subjected to on the microfragment size, we fix the size of the milling ball to 20 mm and the frequency to 30 Hz, and measure the dimensions of microfragments as a function of milling cycles. The average microfragment size decreases with increasing number of milling cycles, reaching a minimum average size of 45 μm after 5 cycles, as shown in Fig. 2b. Unfortunately, even if we subject microfragments to 5 milling cycles, approximately 20% of the microfragments still has at least one dimension above 100 μm, as shown in Fig. 2c. These microfragments risk clogging the printing nozzle, resulting in a discontinuous extrusion, thus affecting the printing resolution. To overcome this limitation, we filter microfragments that have been subjected to 5 milling cycles with a 100 μm nylon mesh to remove bigger particles, as shown in Fig. 2a. The sieved solution contains particles with a lower average size of 20 μm, a more homogeneous size distribution, and hardly any particles with dimensions above 100 μm, as shown in Fig. 2d. Note that despite the filtering process, we still find a few particles with at least one dimension above 100 μm in the solution. We attribute the presence of these rather large particles to their anisotropic shape that lets them penetrate the sieve if favorably aligned.
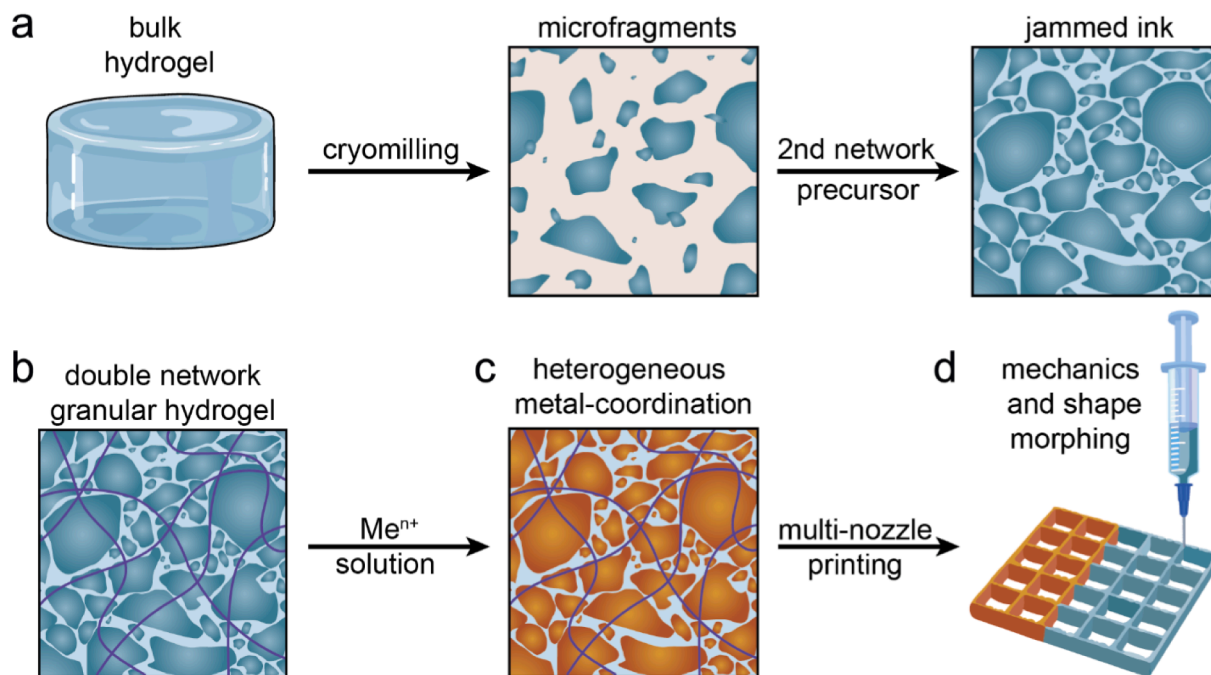
Fig. 1. Fabrication of metal-coordinated DNGHs. **a**, A bulk hydrogel is crosslinked and cryomilled to produce polydisperse microfragments. The obtained microfragments are freeze-dried and resuspended in a monomer-containing solution prior to jamming, yielding a 3D printable ink. **b**, The jammed microfragment paste can be 3D printed and converted into load-bearing DNGHs through UV illumination. **c**, Once crosslinked, the DNGHs are immersed in an ion containing solution to trigger the mechanical reinforcement of the microfragments. **d**, Through multi-nozzle printing, the composition of the DNGHs can be locally varied.
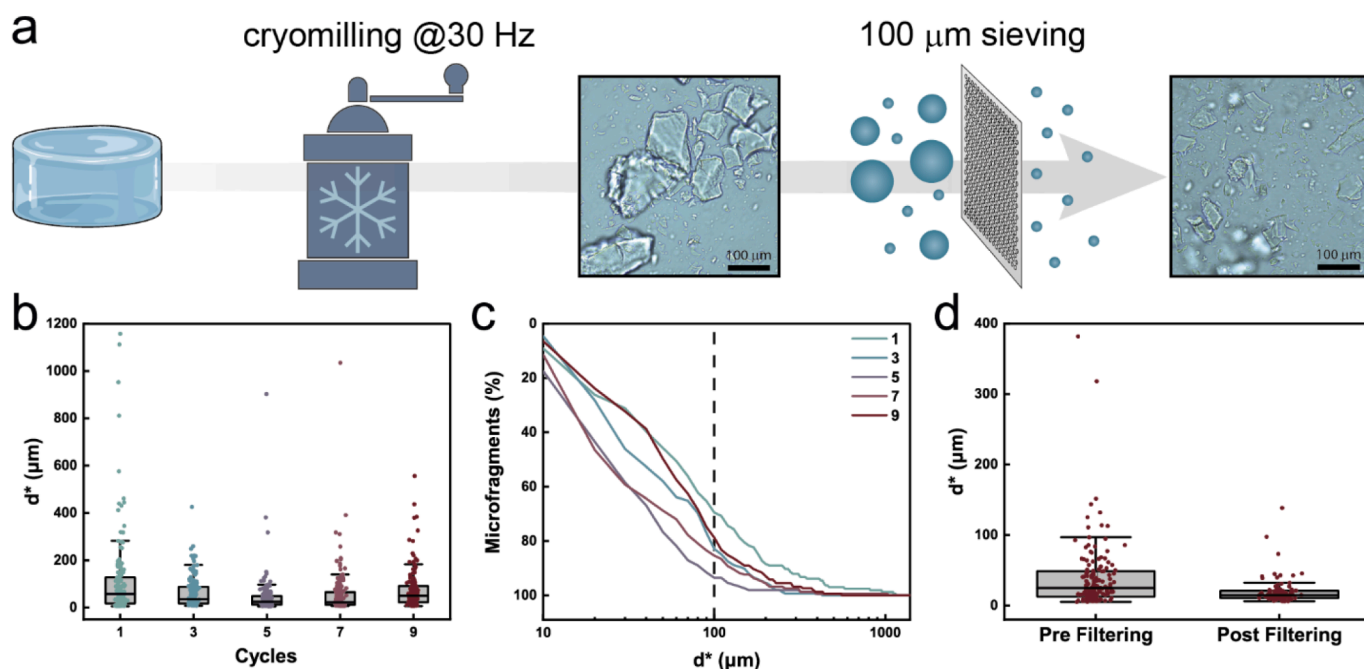
Fig. 2. Fabrication of hydrogel microfragmets through cryomilling. **a**, Schematic illustration of the cryomilling process. A bulk gel is cryomilled at 30 Hz for a certain number of cycles, yielding polydisperse microfragments. The microfragments are filtered through a nylon mesh to remove particles bigger than 100 μm, that would risk clogging the nozzle during the printing process. **b**, Equivalent diameter ($d*$) of microfragments as a function of the milling cycles. Microfragments milled for more than 5 cycles have an average $d*$ of 45 μm. No major improvement in the size or size distribution is observed if microfragments are subjected to more than 5 milling cycles. **c**, Cumulative frequency of microfragment sizes as a function of the milling cycles. Despite the decrease in average $d*$ with increasing milling cycles, around 20% of the microfragments possess diameters larger than 100 μm. **d**, Equivalent diameter of microfragments that have been subjected to 5 milling cycles pre and post filtering. The average $d*$ decreases from 45 μm to 20 μm upon filtration.

However, thanks to the shear alignment of anisotropic particles, we expect them to minimally impact the printability [57,64]. Due to the favorable combination of polydispersity and throughput, filtered microfragments obtained with 5 cycles of cryomilling will be used for all the remaining experiments. The microfragments are freeze-dried prior to further use to ensure longer shelf-life and a better control over their jamming behavior.

To produce an ink composed of jammed microfragments, we resuspend freeze dried microfragments in an aqueous solution containing a second precursor solution. Jammed, soft microparticles, including microgels, display rheological properties that are ideal for extrusion-based 3D printing: they display a low yield stress, a shear-thinning behavior, and a fast shear recovery [47,49,65,66]. Jammed microfragments have shown a similar rheological behavior to that of conventional spherical microgels [44]. To evaluate if this is also the case for our jammed microfragment system that is loaded with reactive monomers, we perform rheology on our ink. We vary the microfragment content in the ink from 10 wt% to 16 wt%, based on the dry polymer weight. To assess the shear-thinning behavior, we perform frequency sweeps as a function of the microfragment weight fraction. All tested samples display a shear-thinning behavior, independent of the microfragment content, as shown in Fig. 3a.

Key to obtaining a good printability is a low extrusion pressure. The extrusion pressure is directly correlated with the yield stress of the ink [67]. To measure the yielding behavior of our inks as a function of the microfragment content contained within them, we perform amplitude sweeps. The yield stress increases from 46 Pa to 2630 Pa, if we increase the microfragment content from 12 wt% to 16 wt%, as shown in Fig. 3b and Fig. S2a. We assign this increase in yield stress to the increased polymer content in the jammed pastes, that results in a higher degree of jamming of the microfragments. Interestingly, the yield point of all measured inks is higher compared to that of inks containing the same weight fraction of jammed spherical microgels, as shown in Fig. S2b.

This difference in yield point is attributed to the mechanical interlocking that is much more pronounced between jammed, non-spherical microfragments than between jammed spherical microparticles, thereby increasing their inter-particle friction [44].

To achieve a high printing fidelity, the ink must quickly recover its solid-like properties upon removal of the shear. To evaluate this property, we perform alternating shear recovery cycles at 1% and 100% strain for 200 s each. All the analyzed inks rapidly transition from the solid-like to the liquid-like state and vice versa, as shown in Fig. 3c. As a result of the favorable rheological properties, the ink can be 3D printed into a grid at a high resolution, as exemplified for an ink containing 16 wt% microfragments in Fig. 3d. To quantify the printing resolution of the microfragment ink, we measure the cross-section of the filament and the area enclosed in the grid as a function of the microfragment concentration. The higher the microfragment concentration, and hence, the higher the degree of jamming, the better is the printing resolution, as shown in Fig. 3e and f. The higher printing resolution comes at the expense of a higher extrusion pressure, as shown in Fig. 3f. We do not have any pressure sensitive component in our ink such that we can maximize the printing resolution by using inks containing 16 wt% of microfragments for the remainder of this study.

Key to the use of hydrogels for load-bearing applications is their ability to withstand significant loads under compression and tension [68,69]. To assess this parameter we quantify the stiffness and work at break of DNGHs composed of PAA microfragments that are firmly connected through an acrylamide network. To transform the rather fragile microfragment-based structure into a mechanically stable DNGH that can bear significant load, we initiate the polymerization of the precursors contained within the microfragments after they have been processed into the appropriate shape, resulting in DNGHs. This is done by exposing the structure to UV light to initiate the radical polymerization reaction of the precursors [49]. The resulting DNGH is soaked in deionized water until it reaches swelling equilibrium. The material is
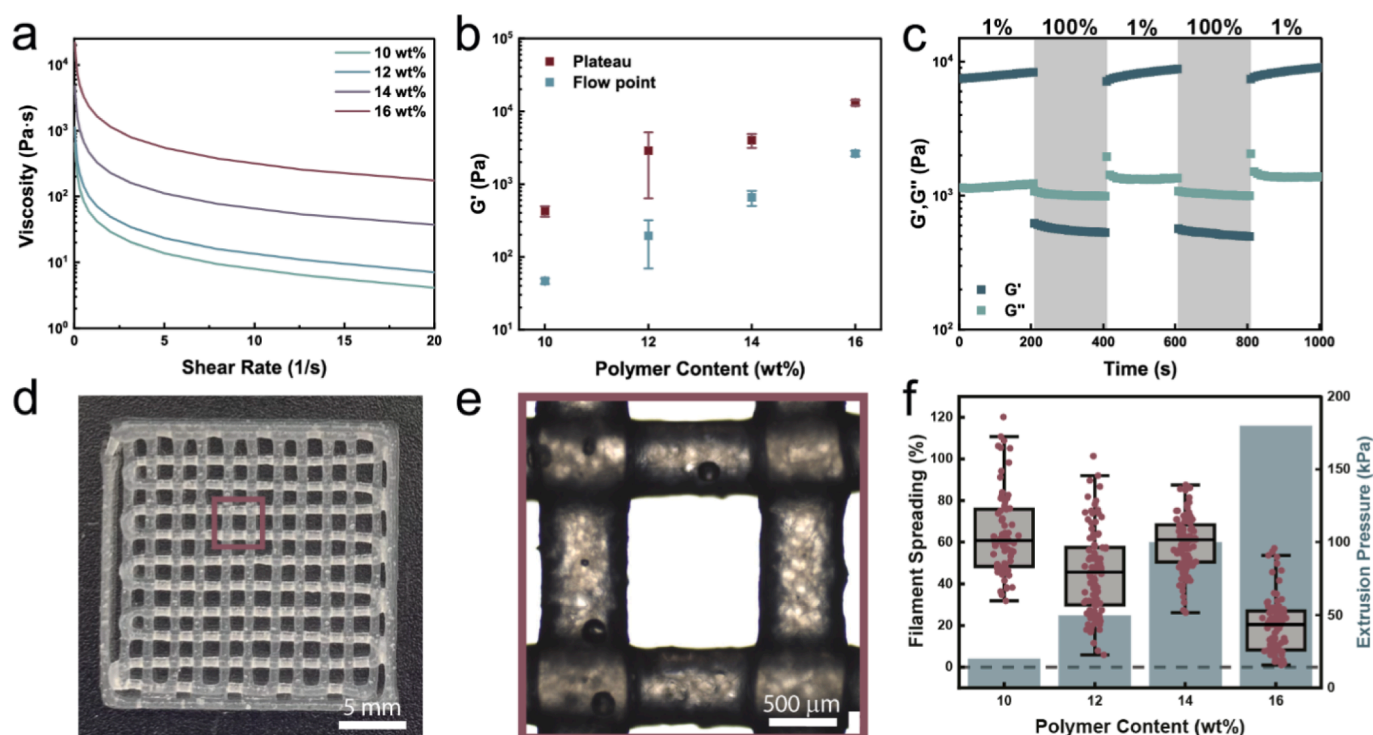
Fig. 3. Printability of jammed microfragments. **a,** Frequency sweep of inks as a function of their microfragment content. All the samples display a decrease in viscosity with increasing shear rate, thus displaying a shear-thinning behavior. **b,** Plateau storage modulus (G', violet) and flow point (red) of inks as a function of their microfragment content. **c,** The shear recovery measurement demonstrates the self-healing behavior of inks containing 16 wt% of PAA microfragments. The material transitions from a solid-like to a liquid-like state when subjected to high shear ($\gamma = 100\%$). The jammed solution recovers rapidly to its initial solid-like condition at low shear ($\gamma = 1\%$). The process can be repeated cyclically without deterioration of the ink performance. **d,** Optical micrograph of a 3D printed grid produced with an ink containing 16 wt% of microfragments. **e,** Optical micrograph of a unit cell of the 3D printed mesh. **f,** Filament spreading (red) and extrusion pressure (grey) as a function of the ink polymer content. An increase in microfragment content in the ink is correlated with a decrease in filament spreading and an increase in extrusion pressure.

relatively soft with a stiffness of 0.16 MPa, and work of fracture of 0.05 $MJ \cdot m^{-3}$. These results are in agreement with previously reported literature on DNGHs composed of spherical microgels [50].

The work of fracture of bulk hydrogels typically increases upon ionic reinforcement [17,70,71]. PAA has a high affinity to certain cations such that it can be ionically reinforced [15,52,72]. To test if ionic reinforcement also increases the work of fracture of our DNGHs, we expose the DNGH to an aqueous solution containing Al^{3+}, as schematically shown in Fig. 1c. Indeed, under compression, the resulting microfragment reinforced DNGHs (mfDNGHs) display a 10-fold increase in compressive modulus, reaching values as high as 1.5 MPa, as shown in Fig. 4a and Fig. S3. Similarly, the Young's modulus measured under tension increases 25-fold upon reinforcement with Al^{3+}, reaching values as high as 4 MPa, as shown in Fig. S4a. The compressive and tensile moduli increase even more, up to 25-fold and 50-fold, respectively, if we reinforce microfragments with Fe^{3+}, as shown in Fig. 4a and Fig. S4a. The great improvement in stiffness is paired with a 16-fold increase in work of fracture with respect to non-reinforced DNGHs, reaching values as high as 0.8 $MJ \cdot m^{-3}$, as shown in Fig. S4b.

Super-elastic, anti-fatigue hydrogels can be obtained if they contain carboxylic ligands and are reinforced with appropriate cations [73,74]. Surprisingly, we do not observe a significant increase in mechanics if we reinforce our mfDNGHs with divalent ions, as shown in Fig. 4a. This behavior is in contrast with PAA metal-reinforced hydrogels reported in literature [52,75]. We attribute the lack of mechanical reinforcement of microfragments upon addition of divalent ions to a stronger complexation between –COOH and –NH_2 groups present in the DNGH, that hinder microfragments from forming complexes with Ca^{2+} and Zn^{2+}. Similarly, monovalent ions, such as Ag^+, do not display any reinforcement effect.

A homogeneous metal reinforcement of charged bulk hydrogels is

difficult to achieve as the diffusivity of metal ions is limited by the electrostatic attraction between the reinforcing ions and the charged hydrogels. This electrostatic attraction leads to a fast formation of a rather dense metal-coordinated hydrogel shell that slows down ion diffusion within this area of the hydrogel [15,76,77]. In addition, the complexed metal ions electrostatically repel free metal ions, thereby further hindering their infiltration into the hydrogel. As a result, there are often gradients in ion concentration within bulk hydrogels that have been ionically reinforced, compromising their mechanical properties [15]. This limitation can, at least to some extent, be overcome by complexing metal ions with weak ligands that undergo competitive ligand exchanges, which reduce the attractive ion-hydrogel interactions [15]. To test if we can increase the extent of ion reinforcement by weakly complexing Fe^{3+} in solution, we incubate our DNGHs in an aqueous solution containing $FeCl_3$ and varying amounts of citric acid (CA). Surprisingly, mfDNGHs display a decrease in compressive modulus with increasing CA concentration, as shown in Fig. 4b and Fig. S5 and summarized in Fig. 4c. A similar trend is observed under uniaxial tensile load, as shown in Fig. S6. This trend is in stark contrast to previously reported bulk metal-reinforced hydrogels, where CA favors a more homogeneous distribution of the ions and thereby improves the overall mechanical performance of these hydrogels [15]. We assign this difference to the granular structure of our gel: ions can more easily diffuse in uncharged PAM networks than in charged PAA networks because of the much reduced or even missing electrostatic attraction between the ions and the uncharged hydrogel. In between the microfragments, our DNGHs are exclusively composed of PAM whereas within the microfragments PAA and PAM networks are present. Hence, we expect ions to more readily diffuse within the PAM single network and hence, between the microfragments. The diffusion path within the charged
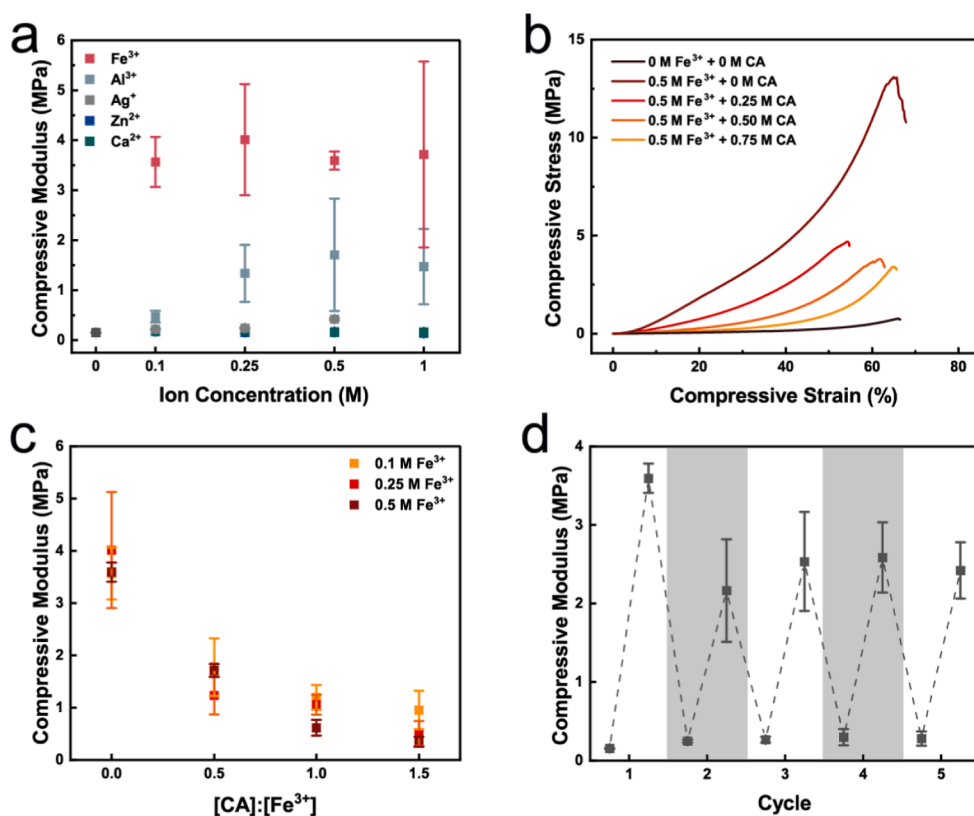
Fig. 4. Mechanical characterization of mfDNGHs. **a**, Compressive modulus of mfDNGHs as a function of the concentration of ions in the incubating solution. If microfragments are reinforced with Fe^{3+} and Al^{3+} the stiffness of mfDNGHs strongly increases. By contrast, the stiffness of mfDNGHs does not significantly change if microfragments are reinforced with mono- or divalent ions (Ca^{2+}, Zn^{2+}, and Ag^+). **b**, Compression curves of DNGHs whose microfragments have been reinforced with Fe^{3+} as a function of the CA concentration. An increase in CA concentration is correlated with a decrease in stiffness. **c**, Compressive modulus of DNGHs whose microfragments have been reinforced with Fe^{3+} as a function of the CA concentration. An increase in CA concentration is paired with a decrease in compressive modulus. **d**, Compressive modulus of DNGHs whose microfragments are repetitively reinforced with Fe^{3+} and weakened with CA.

microfragments is short such that ions can homogeneously reinforce bulk mfDNGHs with dimensions up to 1 cm without the need for any competitive ligand exchanges. This result demonstrates a key advantage of the granular structure: an enhanced diffusivity of charged moieties.

Competitive ligand exchanges are typically used to mechanically reinforce hydrogels. This trick is not needed in our system. However, we still can take advantage of competitive ligand exchanges to selectively remove coordinated Fe^{3+} ions to restore the initial mechanical behavior of DNGHs, as exemplified in Fig. 4d. The mfDNGHs can be repetitively ionically reinforced by incubating them in a solution containing Fe^{3+} and weakened to restore their initial state by exposing them to a CA containing solution, as shown in Fig. 4d. Indeed, the stiffness of mfDNGHs slightly decreases after the first cycle but remains within experimental error unchanged throughout the next four cycles of reinforcement and weakening, as shown in Fig. 4d. The combination of metal-coordination and competitive ligand exchange offers a precise control over the mechanical behavior of mfDNGHs, thus expanding their use in soft actuation.

Our results indicate that the metal reinforcement of microfragments contained in DNGHs strongly increases their stiffness. However, its effect on the work of fracture is limited. The work of fracture of bulk double network hydrogels is typically predominantly determined by the second network [78,79]. Similarly, the work of fracture of purely covalently crosslinked double network granular hydrogels is predominantly determined by the second network as cracks have been shown to preferentially propagate within the interstitial spaces of the microgels [50]. To test if we can increase the work of fracture of DNGHs by ionically reinforcing the matrix network, which constitutes the second network in our system, we fabricate microfragments composed of the uncharged PAM and soak them in an aqueous solution containing acrylic acid. The microfragments are processed into matrix-reinforced double network granular hydrogels (mxDNGHs) using protocols established for mfDNGHs, as schematically shown Fig. 5a and detailed in the experimental section. The compressive modulus of DNGHs increases 8-fold if

their matrix is reinforced with Al^{3+} and 4-fold if the matrix is reinforced with Fe^{3+}, as shown in Fig. 5b. Similarly, the Young's modulus measured under tension reaches values as high as 9 MPa if the matrix is reinforced with Al^{3+}, corresponding to a 75-fold increase relative to non-reinforced DNGHs. A slightly lower stiffness of 3 MPa is achieved if reinforced with Fe^{3+}, as shown in Fig. S7. We assign the higher stiffness of DNGHs whose matrix is reinforced with Al^{3+} compared to those reinforced with Fe^{3+} to the faster binding of Al^{3+}, that leads to a stiffer ionically reinforced shell. These results hint at an inhomogeneous ion distribution within the mxDNGHs.

To test if the ion concentration within mxDNGHs is indeed heterogeneous, we visualize a cross-section of a DNGH whose matrix is reinforced with Fe^{3+}. Indeed, we observe a color gradient along the cross-section of mxDNGHs, in stark contrast to mfDNGHs, as shown in Fig. 5c. This color gradient is indicative of a core–shell structure. This hypothesis is supported by the compression curves of DNGHs whose matrix is reinforced with Fe^{3+} or Al^{3+} that display two distinctly different slopes, as shown in Fig. 5d and Fig. S8.

In bulk hydrogels, gradients in the concentration of ions can be minimized by complexing them with CA as this complexation reduces attractive ion-hydrogel interactions and hence, facilitates the diffusion of ions into the hydrogel [15,76,77]. To test if this is also the case for our DNGHs possessing a PAA matrix, we incubate them in an aqueous solution containing Fe^{3+} and varying concentrations of CA. If incubated in a solution containing 0.5 M Fe^{3+} and 0.75 M CA, mxDNGHs are homogeneously colored. These results suggest that the complexation of Fe^{3+} with CA increases the homogeneity of Fe^{3+} ions within the mxDNGHs. The metal reinforcement introduces some sample-to-sample variability, which results in large error bars. We assign this variability to differences in the ion diffusion within samples with slightly different microstructures. Nevertheless, we observe a statistically relevant increase in compressive modulus with increasing CA concentration contained in the incubating solution until it reaches 3 MPa, as shown in Fig. 5e. An analogous behavior is observed under tensile testing, where
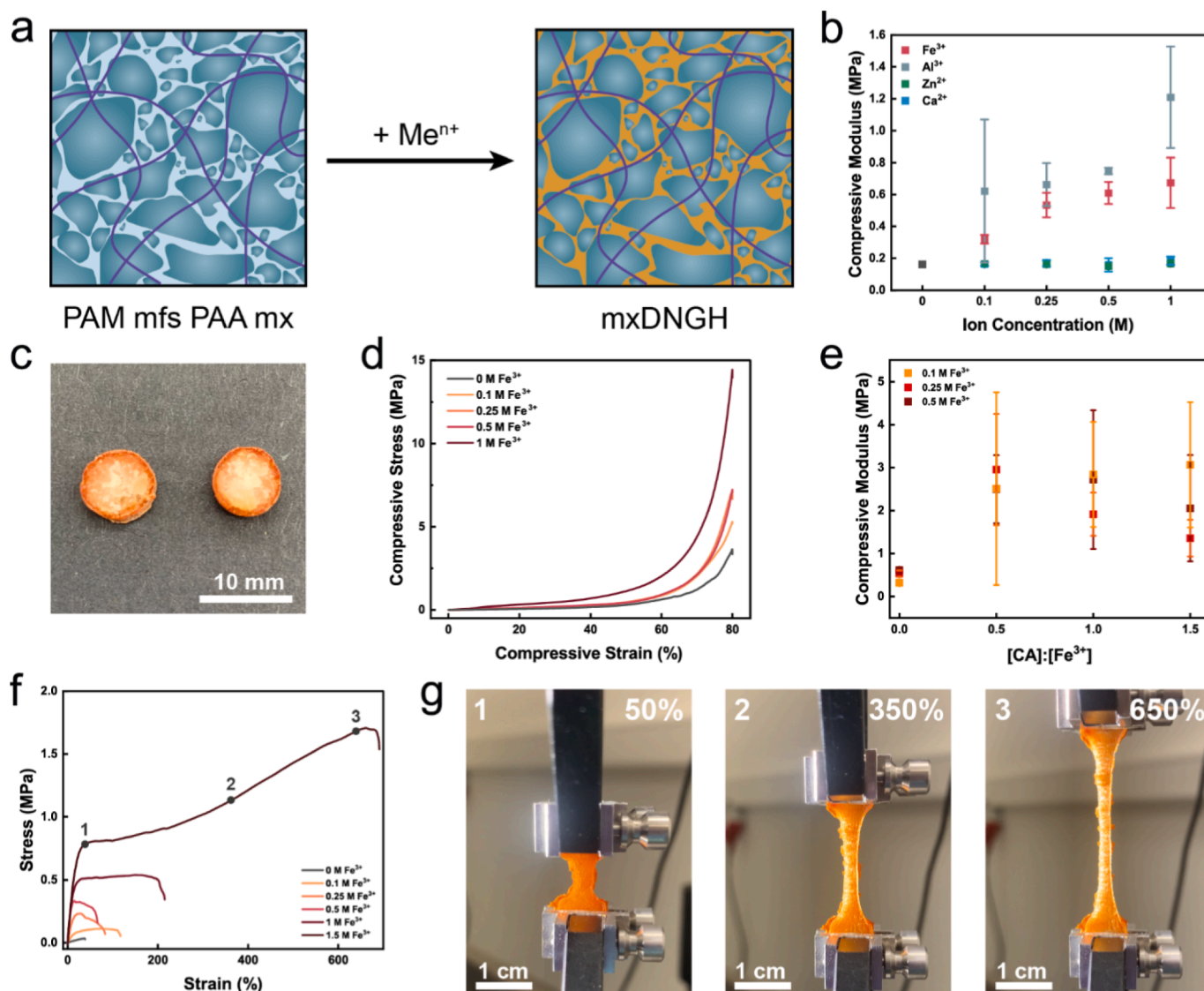
Fig. 5. Mechanical characterization of mxDNGHs. **a**, A DNGH is composed of PAM microfragments and a PAA matrix. The matrix is selectively reinforced with ions, yielding a mxDNGH. **b**, Compressive modulus of mxDNGHs as a function of the ion concentration present in the reinforcing solution. Fe^{3+} and Al^{3+} increase the stiffness of mxDNGH, whereas no appreciable changes are observed for DNGHs whose matrix is reinforced with Ca^{2+}, Zn^{2+}, and Ag^+. **c**, Optical photograph of a mxDNGH cylinder. The color gradient is a clear indication of a non-homogeneous ionic reinforcement. **d**, Compression curves of DNGHs whose matrix is reinforced with Fe^{3+} as a function of the Fe^{3+} concentration in the reinforcing solution. All curves display an initial soft behavior, followed by a stiffening. This change in stiffness is indicative of a core–shell structure. **e**, Compression modulus of mxDNGHs whose matrix is reinforced with Fe^{3+} as a function of the CA concentration. An increase in CA concentration is paired with a steep increase in compression modulus. The CA slows down the ionic complexation, thus producing more homogeneous, stiffer structures. **f**, Tensile curves of mxDNGHs as a function of the Fe^{3+} concentration in the reinforcing solution. Higher Fe^{3+} concentrations in the incubating solution result in a more pronounced yielding plateau of mxDNGHs, characteristic of the formation of a core–shell structure. **g**, Time lapse of a mxDNGH whose matrix is reinforced with Fe^{3+}. Initially the sample displays a homogeneous texture (1). Once the mxDNGH is pulled above its yield point, the hard shell cracks (2), and a softer stretchy core is revealed (3).

the stiffness of mxDNGHs increases with the CA concentration in the ion-containing solution, until it reaches Young's moduli as high as 25 MPa, as shown in Fig. S10. Interestingly, when the molar ratio of [CA]: [Fe^{3+}] exceeds 0.5, the Young's modulus decreases. This behavior is attributed to the large excess of carboxylic groups in the CA solution with respect to the carboxylic groups present in the PAA network that reduces the number of Fe^{3+} ions complexed within the PAA matrix.

The increase in stiffness is paired with a strong decrease in strain at break, as shown in Fig. S11. The decrease in strain at break typically reduces the toughness of soft materials rendering them more fragile. To test if this is also the case for our system, we extract the work of fracture as a function of the molar ratio of [CA]: [Fe^{3+}] by quantifying the area under the stress–strain curve. Interestingly, the work of fracture remains

almost unchanged with values around 0.20 MJ·m^{-3}. This result is in agreement with previously reported literature on metal-reinforced bulk hydrogels and demonstrates the potential of these systems [15].

Metal-coordination increases the stiffness and toughness of dually crosslinked hydrogels by introducing physical crosslinks in a pre-existing covalent network [72]. However, the increased crosslink density comes at the expense of the water content: upon metal-reinforcement, hydrogels typically undergo syneresis, resulting in their shrinkage. To assess to what extent our mrDNGHs undergo syneresis, we quantify the water content of all our samples by gravimetric analysis as a function of the ion concentration present within the reinforcing solution. As expected, an increase in ion concentration within the mrDNGHs is paired with a decrease in their water content, reaching values as low as

24 wt% when mxDNGHs have been exposed to aqueous solutions containing 1.5 M of $AlCl_3$, as shown in Fig. S12.

Our results indicate that an increased density of ionic crosslinks directly correlates with a reduction in water content within these hydrogels. While this behavior can be detrimental for cell work, it can be exploited as an asset in the fabrication of load-bearing tough hydrogels. Indeed, the shrinkage induced by the secondary crosslinking with metal ions forces the polymer chains to collapse, thus increasing their hidden length, and hence, the fracture toughness of the hydrogel [9]. Nature frequently leverages this behavior to build hydrogel-based materials displaying an unparalleled toughness [2,6,80]. To test if we can promote this behavior in our mxDNGHs, we reinforce them with Fe^{3+} in the absence of CA to create a stiff shell that shrinks, thereby mechanically forcing the core contained within the shell to also collapse. Indeed, we observe two distinctly different slopes in the stress–strain curves of samples that have been reinforced with solutions containing Fe^{3+} concentrations ≥ 1 M, as shown in Fig. 5f, Fig. 5g. The two distinctly different slopes in the stress–strain curves of these DNGHs, which translate into two distinctly different stiffnesses, indicate that they possess core–shell structures: DNGHs whose matrix is reinforced with high concentrations of Fe^{3+} display an initial stiff behavior if put under tension, which we assign to the stiff Fe^{3+} reinforced shell. This initial steep increase in the stress–strain curve is followed by a clear yielding plateau, indicative of the much softer core, as supported by visualizing the sample deformation during tensile-tests in Movie M1. A similar behavior is observed when the matrix of DNGHs is reinforced with Al^{3+}, as shown in Fig. S13. Overall, the fracture strength and strain at break of mxDNGHs increase with increasing ion concentration within the reinforcing solution, resulting in a stiffness as high as 9 MPa and a work of fracture as high as 12 MJ·m^{-3}, as shown in Fig. S7, Fig. S9.

To evaluate the overall mechanical performance of mfDNGHs and mxDNGHs, we compare our material with state-of-the-art 3D printed hydrogels. Remarkably, our material possesses values of stiffnesses and work of fractures that are higher than any previously reported 3D printed hydrogel, as summarized in Fig. 6a. To assess if the excellent mechanical properties are solely related to the high polymer content, we compare our formulations and previously reported 3D printed hydrogels as a function of their polymer content. Even if we compare our material to hydrogels possessing a similar polymer content, they are still significantly stiffer and tougher than any previously reported 3D printed hydrogel, as summarized in Fig. 6b and Fig. 6c. These results highlight the potential of our 3D printable hydrogels for load-bearing applications.

To demonstrate the synergistic combination of 3D printing and metal-coordination of mfDNGHs, we 3D print a hinge, as shown in Fig. 7a that we reinforce with Fe^{3+}, as shown in Fig. 7b. The reinforced hinge with a cross-section of 0.36 cm^2 holds up to 1.5 kg of weight without any appreciable damage, as shown in Fig. 7c. This example demonstrates the potential of 3D printed mfDNGHs as load-bearing structures.

Our results demonstrate that metal coordination of the matrix leads to an increase in the crosslink density of the hydrogel, which results in the expulsion of significant amounts of water and hence, leads to a shrinkage of the mrDNGHs. We exploit this volume change to 4D print shape morphing structures: we trigger conformational changes of 3D printed structures with spatially varying compositions through their exposure to an aqueous solution containing reinforcing Fe^{3+} ions. We fabricate structures possessing areas that are composed of PAA microfragments and others made of inert PAM microfragments that cannot be ionically crosslinked and hence, do not shrink upon incubation in a Fe^{3+}-containing solution, as shown in Fig. 7d and e. Indeed, upon exposure to a $FeCl_3$ containing solution, areas composed of PAA microfragments significantly shrink due to the ion reinforcement of these structures. By contrast, areas composed of PAM fragments do not significantly change their volumes. As a result of the difference in the swelling behavior, we trigger the shape-morphing of the printed structures, as shown in Fig. 7f and g. This shape morphing is in good agreement with the behavior simulated using Abaqus, as shown in Fig. 7h and i.

3. Conclusion

We introduce 3D printable metal reinforced DNGHs, which display stiffnesses and toughnesses that exceed those of any previously reported 3D printed hydrogel at least 9-fold. By choosing appropriate reinforcing ions, we can tune the mechanical properties of these DNGHs to be similar to some stiff and tough natural polymer-based materials, such as cartilage and tendons. The fabrication of microfragments through cryo-omilling holds great potential for their use in materials that are produced at large scales thanks to its scalability and the possibility to process a wide range of materials. We leveraged the freedom in the material selection offered by this technique to selectively render certain areas of hydrogels responsive to metal ions. The selective binding of metal ions to PAA enables a targeted reinforcement of 3D printed structures without the need to trade off stiffness and toughness. We envisage the combination of good processability, high stiffness and toughness of these materials to open up new fields of use of these hydrogels, that are significantly stiffer and stronger than previously reported 3D printable counterparts. Thanks to their load-bearing properties, we foresee these materials to open up new possibilities to fabricate the next generation of load-bearing soft robots capable of
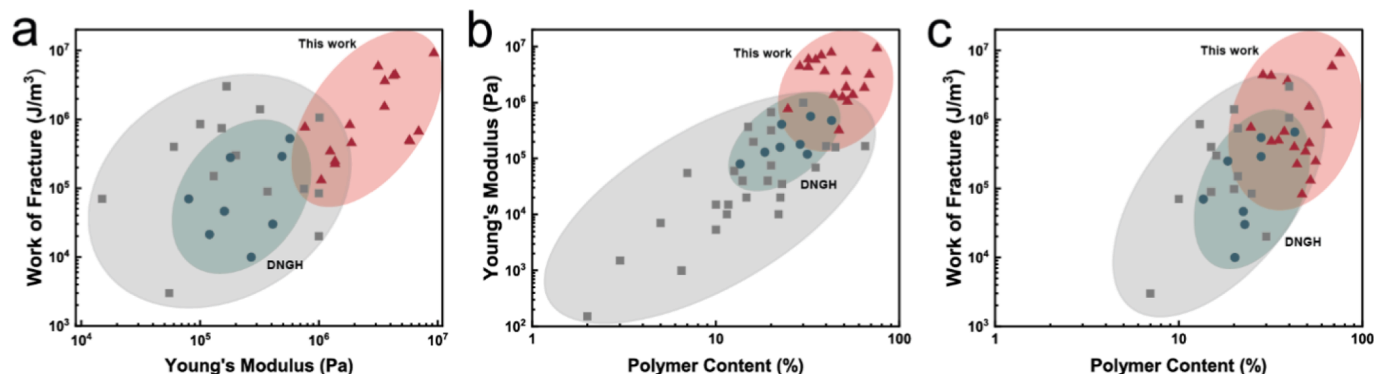

Fig. 6. Ashby plots of 3D printed hydrogels. **a**, Ashby plot of the work of fracture of 3D printed hydrogels as a function of their Young's modulus. Our material possesses a synergistic combination of high stiffness and high work of fracture, a seemingly counteracting set of properties. **b**, Ashby plot of the Young's modulus of 3D printed hydrogels as a function of their polymer content. mf- and mxDNGHs display higher stiffnesses compared to any previously reported 3D printed hydrogel. **c**, Ashby plot of the work of fracture of 3D printed hydrogels as a function of their polymer content. mfDNGHs and mxDNGHs display a higher work of fracture compared to any previously reported 3D printed hydrogel. Gray shaded areas collect state-of-the-art mechanics of load-bearing 3D printed hydrogels; green shaded areas represent mechanics of non-reinforced DNGHs; red shaded areas summarize mechanics of mfDNGHs and mxDNGHs.
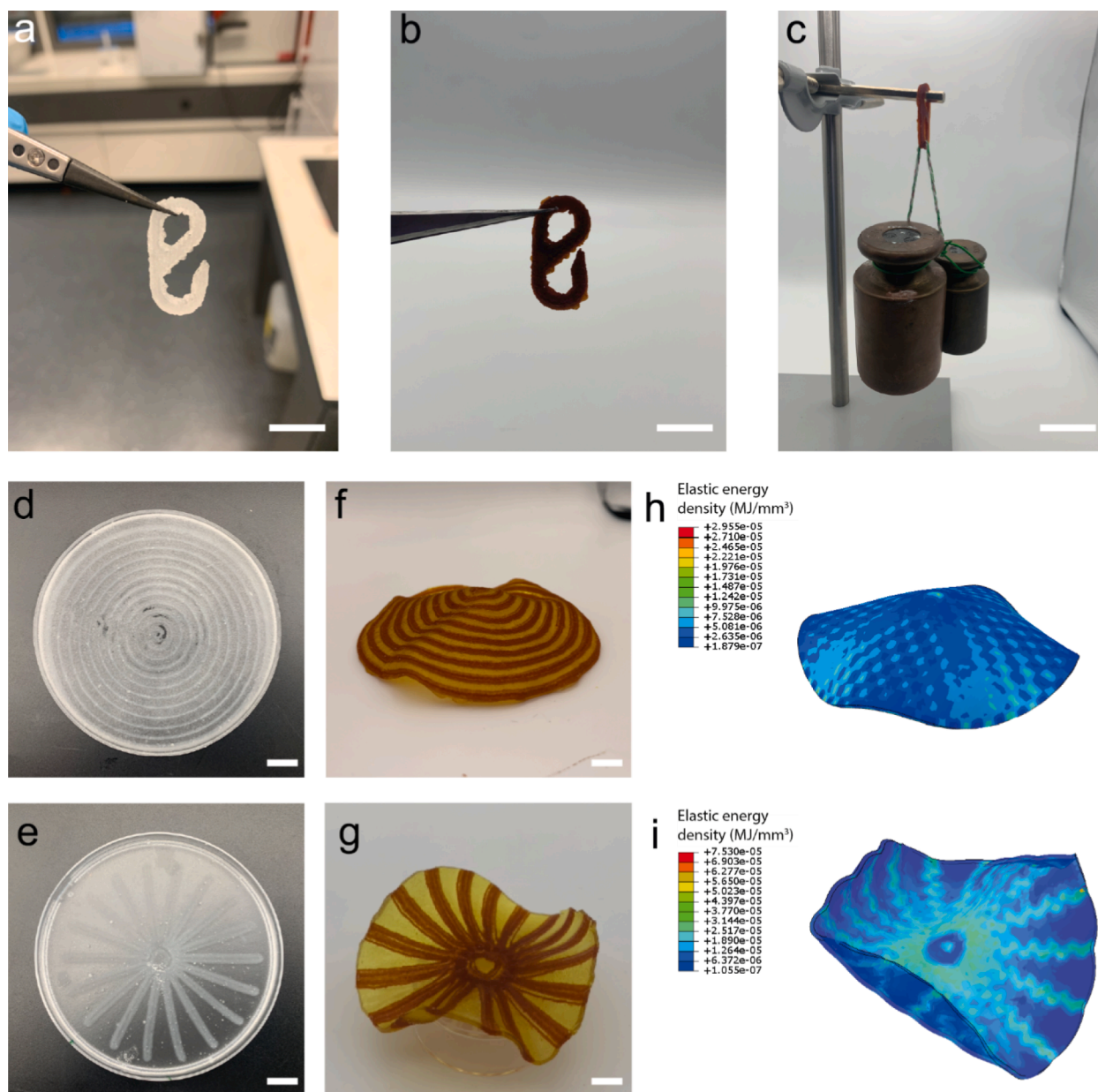
Fig. 7. Applications of 3D printed mfDNGHs. **a,b**, Photographs of a 3D printed mfDNGH hinge (**a**) before and (**b**) after reinforcement with Fe^{3+}. Scale bar is 2 cm. **c**, Photograph of a mfDNGH hinge holding 1.5 kg of weight. Scale bar is 5 cm. **d-i**, 4D printing of shape-morphing mfDNGHs. (**d,e**) Photographs of 3D printed DNGHs composed of DNGHs whose microfragments have been reinforced with Fe^{3+} (red) and others that have not been reinforced with ions (yellow). (**f,g**) Photographs of the shape-morphed structures, and (**h,i**) corresponding Abaqus simulations. Scale bars are 1 cm.

undergoing more complex movements than what is currently possible. With additional work devoted to adapting their composition to render them biocompatible, we envisage these materials to even be used as tissue replacements.

4. Methods

4.1. Materials

Acrylic acid (AA) (Sigma-Aldrich, 147230), acrylamide (AM) (Sigma-Aldrich, A4058), N,N'-methylene bisacrylamide (MBA) (Carl Roth, 7867.1), 2-hydroxy-2-methylpropiophenone (PI) (Sigma-Aldrich, 405655), mineral oil light (Sigma-Aldrich, 330779), Span80 (TCI Chemicals, S0060), iron (III) chloride (Sigma-Aldrich, 451649), aluminum chloride (Sigma-Aldrich, 563919), calcium chloride (Sigma-Aldrich, 499609), zinc chloride (Sigma-Aldrich, 208086), silver nitrate

(Sigma-Aldrich, 209139), citric acid (Sigma-Aldrich, 251275), ethanol (Sigma-Aldrich, 459844), are all used as received.

4.2. Preparation of PAA and PAM hydrogels

An aqueous solution containing 30 wt% of monomer (AA or AM), 1 wt% MBA crosslinker and 5 mg/mL of PI is prepared. The solution is poured in a Petri dish ($d = 20$ cm) and polymerized for 5 min in an UV oven (UVChamber-365-100, UWave, 25 mW/cm^2) yielding a bulk hydrogel.

4.3. Preparation of microfragments

The bulk hydrogel is crushed using a commercial blender and dispersed in water to reach swelling equilibrium. The resulting hydrogel fragments are frozen in liquid nitrogen (LN2) before they are cryomilled

with an oscillatory cryomill (Cryomill, Retsch) using 12 stainless steel balls ($d = 10$ mm). The cryomilling protocol is as follows: 3 min of pre-cooling; 5 milling cycles of 3 min at 30 Hz; 30 s at 5 Hz between each cycle, unless stated differently. The resulting microfragments are suspended in water and filtered with a nylon filter of 100 μm mesh to remove bigger fragments. The microfragments are freeze-dried and stored in powder form until further use.

4.4. Preparation of microgels

PAA microgels are prepared following a protocol reported in literature [49]. Briefly, an aqueous solution containing 30 wt% AA, 1 wt% MBA, and 5 mg/mL PI is prepared. The aqueous phase is emulsified in a 5:1 volume ratio with a mineral oil-based solution containing 2 wt% Span80. The water-in-oil emulsion is stirred while being illuminated with UV light (OmniCure S1000, Lumen Dynamics, 320-390 nm, 60 mW/cm^2) for 5 min to convert drops into microgels. The resulting PAA microgels are transferred into ethanol and centrifuged at 4500 rpm for 10 min (Mega Star 1.6R, VWR) to remove the oil. The supernatant is discarded, and the process is repeated three times with ethanol and three times with water. Clean PAA microgels are resuspended in water for storage.

4.5. Rheology of microfragments

Rheology measurements are performed on a DHR-3 TA Instrument with an 8 mm diameter parallel plate steel geometry. All measurements are performed at 25 °C, with an 800 μm gap. The samples are allowed to relax for 200 s before each measurement. Frequency dependent viscosity measurements are performed at 0.5% strain. Amplitude sweeps are performed at 1.0 rad/s oscillation. Self-healing measurements are performed at 1.0 rad/s, alternating 200 s at 1% strain, with 200 s at 100% strain.

4.6. 3D printing of microfragments

The jammed microfragment paste is loaded in a 3 mL Luer lock syringe. The syringe is sealed and centrifuged at 4500 rpm for 5 min to remove trapped air bubbles that would affect the printing quality. 3D printing is performed with a commercial 3D bioprinter (BIO X, Cellink) at 10 mm/s and 100 kPa, unless stated differently. The granular ink is extruded from a conical nozzle (22 G, inner diameter 0.41 mm) through a pressure driven piston.

4.7. Preparation of mfDNGH

PAA microfragments are suspended in an aqueous solution containing 30% AM, 0.5 wt% MBA and 5 mg/mL of PI. After centrifuging microfragments at 4500 rpm for 10 min and removing the supernatant, a jammed paste is obtained. The paste is casted into dog-bone shaped molds (cross-section 5×2 mm^2) or cylindrical molds ($d = 5$ mm, $t = 5$ mm), and crosslinked for 5 min under UV irradiation (UVChamber-365-100, UWave, 25 mW/cm^2).

4.8. Preparation of mxDNGH

PAM microfragments are suspended in an aqueous solution containing 30% AA, 0.5 wt% MBA and 5 mg/mL of PI. The same procedure used to prepare mfDNGH is applied.

4.9. Mechanical characterization of mfDNGH and mxDNGH

Mechanical measurements are performed with a commercial machine (zwickiLine 5 kN, 50 N load cell, Zwick Roell). Compression tests are performed on cylindrical samples (d = 8 mm, h = 8 mm), compressed at a constant velocity of 3 mm/min until fracture or 80% strain

is reached. The compressive modulus is calculated as the slope of the region from 0% to 5% strain. Tensile tests are performed on dog-bone shaped samples (cross-section of the gauge: 5×2 mm^2), stretched at a constant velocity of 100 mm/min. The Young's modulus is calculated as the slope of the initial linear region, from 5% to 15% strain. The work of fracture (WOF) is calculated as the area below the stress-strain curve.

4.10. Shape-morphing simulation

The shape-morphing properties are analyzed using Finite Element Modelling (FEM), specifically via the software package Abacus, which allows for simulation of structures with spatially varying volume changes. The areas of the shape-morphing structures corresponding to the mrDNGHs are represented by linear beam elements (Abacus Beam Elements B31), with the non-reinforced DNGHs represented with quadratic tetrahedron elements (Abacus Tetrahedron Elements C3D10). The areas of mrDNGHs are embedded within the soft phase, and the active material's shrinkage is assumed to be linearly related to the applied load with an expansion ratio of -0.0016 and a field load range of 1-100. To simulate the evolution of the shape morphing, the active and soft phases are initialized at the same elastic modulus and that of the reinforced areas is gradually increased by factor of fifteen.

Declaration of Competing Interest

The authors declare the following financial interests/personal relationships which may be considered as potential competing interests: Esther Amstad reports financial support was provided by Swiss National Science Foundation.

Data availability

Data will be made available on request.

Acknowledgements

Author contributions

M. H. and L. D. performed the experiments. Q. G., and J. H. performed the simulations. M. H., L. D., and E. A. discussed the results. M. H. and E. A. designed the study, and prepared the manuscript.

Appendix A. Supplementary data

Supplementary data to this article can be found online at https://doi.org/10.1016/j.cej.2023.145433.

References

[1] L. Ng, M.A. Elgar, D. Stuart-Fox, From bioinspired to bioinformed: benefits of greater engagement from biologists, accessed August 15, 2022, Front. Ecol. Evol. 9 (2021), https://www.frontiersin.org/articles/10.3389/fevo.2021.790270.

[2] M.J. Harrington, F. Jehle, T. Priemel, Mussel byssus structure-function and fabrication as inspiration for biotechnological production of advanced materials, Biotechnol. J. 13 (2018) 1800133, https://doi.org/10.1002/biot.201800133.

[3] C.N.Z. Schmitt, Y. Politi, A. Reinecke, M.J. Harrington, Role of sacrificial protein-metal bond exchange in mussel byssal thread self-healing, Biomacromolecules 16 (2015) 2852–2861, https://doi.org/10.1021/acs.biomac.5b00803.

[4] M.J. Harrington, A. Masic, N. Holten-Andersen, J.H. Waite, P. Fratzl, Iron-clad fibers: a metal-based biological strategy for hard flexible coatings, Science 328 (2010) 216–220, https://doi.org/10.1126/science.1181044.

[5] M. Krogsgaard, V. Nue, H. Birkedal, Mussel-inspired materials: self-healing through coordination chemistry, Chem. – Eur. J. 22 (2016) 844–857, https://doi.org/10.1002/chem.201503380.

[6] S. Zechel, M.D. Hager, T. Priemel, M.J. Harrington, Healing through histidine: bioinspired pathways to self-healing polymers via imidazole-metal coordination, Biomimetics. 4 (2019) 20, https://doi.org/10.3390/biomimetics4010020.

[7] A. Charlet, F. Bono, E. Amstad, Mechanical reinforcement of granular hydrogels, Chem. Sci. 13 (2022) 3082–3093, https://doi.org/10.1039/D1SC06231J.

[8] X. Zhao, Multi-scale multi-mechanism design of tough hydrogels: building dissipation into stretchy networks, Soft Matter 10 (2014) 672–687, https://doi.org/10.1039/C3SM52272E.

[9] X. Zhao, X. Chen, H. Yuk, S. Lin, X. Liu, G. Parada, Soft materials by design: unconventional polymer networks give extreme properties, Chem. Rev. 121 (2021) 4309–4372, https://doi.org/10.1021/acs.chemrev.0c01088.

[10] J. Jin, L. Cai, Y.-G. Jia, S. Liu, Y. Chen, L. Ren, Progress in self-healing hydrogels assembled by host– guest interactions: preparation and biomedical applications, J. Mater. Chem. B 7 (2019) 1637–1651, https://doi.org/10.1039/C8TB02547A.

[11] C. Li, M.J. Rowland, Y. Shao, T. Cao, C. Chen, H. Jia, X. Zhou, Z. Yang, O. A. Scherman, D. Liu, Responsive double network hydrogels of interpenetrating dna and cb[8] host-guest supramolecular systems, Adv. Mater. 27 (2015) 3298–3304, https://doi.org/10.1002/adma.201501102.

[12] J. Chen, R. An, L. Han, X. Wang, Y. Zhang, L. Shi, R. Ran, Tough hydrophobic association hydrogels with self-healing and reforming capabilities achieved by polymeric core-shell nanoparticles, Mater. Sci. Eng. C 99 (2019) 460–467, https://doi.org/10.1016/j.msec.2019.02.005.

[13] L. Xu, X. Zhao, C. Xu, N.A. Kotov, Water-rich biomimetic composites with abiotic self-organizing nanofiber network, Adv. Mater. 30 (2018) 1703343, https://doi.org/10.1002/adma.201703343.

[14] A. Andersen, M. Krogsgaard, H. Birkedal, Mussel-inspired self-healing double-cross-linked hydrogels by controlled combination of metal coordination and covalent cross-linking, Biomacromolecules 19 (2018) 1402–1409, https://doi.org/10.1021/acs.biomac.7b01249.

[15] M. Hirsch, M. Steinacher, R. Zhao, E. Amstad, Load-bearing hydrogels ionically reinforced through competitive ligand exchanges, Biomater. Sci. 9 (20) (2021) 6753–6762.

[16] A. Charlet, V. Lutz-Bueno, R. Mezzenga, E. Amstad, Shape retaining self-healing metal-coordinated hydrogels, Nanoscale 13 (7) (2021) 4073–4084.

[17] S.Y. Zheng, H. Ding, J. Qian, J. Yin, Z.L. Wu, Y. Song, Q. Zheng, Metal-coordination complexes mediated physical hydrogels with high toughness, stick-slip tearing behavior, and good processability, Macromolecules 49 (2016) 9637–9646, https://doi.org/10.1021/acs.macromol.6b02150.

[18] A. Charlet, M. Hirsch, S. Schreiber, E. Amstad, Recycling of load-bearing 3d printable double network granular hydrogels, Small 18 (12) (2022) 2107128.

[19] N. Zheng, Y. Xu, Q. Zhao, T. Xie, Dynamic covalent polymer networks: a molecular platform for designing functions beyond chemical recycling and self-healing, Chem. Rev. 121 (2021) 1716–1745, https://doi.org/10.1021/acs.chemrev.0c00938.

[20] P. Fratzl, R. Weinkamer, Nature's hierarchical materials, Prog. Mater Sci. 52 (2007) 1263–1334, https://doi.org/10.1016/j.pmatsci.2007.06.001.

[21] C. Chen, Y. Kuang, S. Zhu, I. Burgert, T. Keplinger, A. Gong, T. Li, L. Berglund, S. J. Eichhorn, L. Hu, Structure–property–function relationships of natural and engineered wood, Nat. Rev. Mater. (2020) 1–25, https://doi.org/10.1038/s41578-020-0195-z.

[22] P. Fratzl, Biomimetic materials research: what can we really learn from nature's structural materials? J. R. Soc. Interface 4 (2007) 637–642, https://doi.org/10.1098/rsif.2007.0218.

[23] A.S. Caldwell, G.T. Campbell, K.M.T. Shekiro, K.S. Anseth, Clickable microgel scaffolds as platforms for 3d cell encapsulation, Adv. Healthc. Mater. 6 (2017) 1700254, https://doi.org/10.1002/adhm.201700254.

[24] A.C. Daly, L. Riley, T. Segura, J.A. Burdick, Hydrogel microparticles for biomedical applications, Nat. Rev. Mater. 5 (2020) 20–43, https://doi.org/10.1038/s41578-019-0148-6.

[25] J.M. Lowen, J.K. Leach, Functionally graded biomaterials for use as model systems and replacement tissues, Adv. Funct. Mater. 30 (2020) 1909089, https://doi.org/10.1002/adfm.201909089.

[26] F. Jehle, P. Fratzl, M.J. Harrington, Metal-tunable self-assembly of hierarchical structure in mussel-inspired peptide films, ACS Nano 12 (2018) 2160–2168, https://doi.org/10.1021/acsnano.7b07905.

[27] H. Tan, C. Xiao, J. Sun, D. Xiong, X. Hu, Biological self-assembly of injectable hydrogel as cell scaffold via specific nucleobase pairing, Chem. Commun. 48 (2012) 10289–10291, https://doi.org/10.1039/C2CC35449G.

[28] R. Blell, X. Lin, T. Lindström, M. Ankerfors, M. Pauly, O. Felix, G. Decher, Generating in-plane orientational order in multilayer films prepared by spray-assisted layer-by-layer assembly, ACS Nano 11 (2017) 84–94, https://doi.org/10.1021/acsnano.6b04191.

[29] W. Li, P. Zhao, C. Lin, X. Wen, E. Katsanevakis, D. Gero, O. Félix, Y. Liu, Natural polyelectrolyte self-assembled multilayers based on collagen and alginate: stability and cytocompatibility, Biomacromolecules 14 (2013) 2647–2656, https://doi.org/10.1021/bm4005063.

[30] S. Cha, H.G. Lim, M.F. Haase, K.J. Stebe, G.Y. Jung, D. Lee, Bicontinuous interfacially jammed emulsion gels (bijels) as media for enabling enzymatic reactive separation of a highly water insoluble substrate, Sci. Rep. 9 (2019) 6363, https://doi.org/10.1038/s41598-019-42769-8.

[31] G. Di Vitantonio, T. Wang, M.F. Haase, K.J. Stebe, D. Lee, Robust bijels for reactive separation via silica-reinforced nanoparticle layers, ACS Nano 13 (2019) 26–31, https://doi.org/10.1021/acsnano.8b05718.

[32] W. Lei, S. Qi, Q. Rong, J. Huang, Y. Xu, R. Fang, K. Liu, L. Jiang, M. Liu, Diffusion–freezing-induced microphase separation for constructing large-area multiscale structures on hydrogel surfaces, Adv. Mater. 31 (2019) 1808217, https://doi.org/10.1002/adma.201808217.

[33] G.-L. Ying, N. Jiang, S. Maharjan, Y.-X. Yin, R.-R. Chai, X. Cao, J.-Z. Yang, A. K. Miri, S. Hassan, Y.S. Zhang, Aqueous two-phase emulsion bioink-enabled 3d bioprinting of porous hydrogels, Adv. Mater. 30 (2018) 1805460, https://doi.org/10.1002/adma.201805460.

[34] W. Jia, P.S. Gungor-Ozkerim, Y.S. Zhang, K. Yue, K. Zhu, W. Liu, Q. Pi, B. Byambaa, M.R. Dokmeci, S.R. Shin, A. Khademhosseini, Direct 3D bioprinting of perfusable vascular constructs using a blend bioink, Biomaterials 106 (2016) 58–68, https://doi.org/10.1016/j.biomaterials.2016.07.038.

[35] M. Kessler, H. Elettro, I. Heimgartner, S. Madasu, K.A. Brakke, F. Gallaire, E. Amstad, Everything in its right place: controlling the local composition of hydrogels using microfluidic traps, Lab Chip 20 (24) (2020) 4572–4581.

[36] H. Du, A. Cont, M. Steinacher, E. Amstad, Fabrication of hexagonal-prismatic granular hydrogel sheets, Langmuir 34 (2018) 3459–3466, https://doi.org/10.1021/acs.langmuir.7b04163.

[37] D. Chimene, C.W. Peak, J.L. Gentry, J.K. Carrow, L.M. Cross, E. Mondragon, G. B. Cardoso, R. Kaunas, A.K. Gaharwar, Nanoengineered ionic-covalent entanglement (nice) bioinks for 3d bioprinting, ACS Appl. Mater. Interfaces 10 (2018) 9957–9968, https://doi.org/10.1021/acsami.7b19808.

[38] G. Ying, N. Jiang, C. Parra-Cantu, G. Tang, J. Zhang, H. Wang, S. Chen, N.-P. Huang, J. Xie, Y.S. Zhang, Bioprinted injectable hierarchically porous gelatin methacryloyl hydrogel constructs with shape-memory properties, Adv. Funct. Mater. 30 (2020) 2003740, https://doi.org/10.1002/adfm.202003740.

[39] R. Levato, T. Jungst, R.G. Scheuring, T. Blunk, J. Groll, J. Malda, From shape to function: the next step in bioprinting, Adv. Mater. 32 (2020) 1906423, https://doi.org/10.1002/adma.201906423.

[40] K.S. Lim, R. Levato, P.F. Costa, M.D. Castilho, C.R. Alcala-Orozco, K.M.A. van Dorenmalen, F.P.W. Melchels, D. Gawlitta, G.J. Hooper, J. Malda, T.B. F. Woodfield, Bio-resin for high resolution lithography-based biofabrication of complex cell-laden constructs, Biofabrication 10 (2018), 034101, https://doi.org/10.1088/1758-5090/aac00c.

[41] L. Aydin, S. Kucuk, H. Kenar, A universal self-eroding sacrificial bioink that enables bioprinting at room temperature, Polym. Adv. Technol. 31 (7) (2020) 1634–1647.

[42] A.C. Daly, M.D. Davidson, J.A. Burdick, 3D bioprinting of high cell-density heterogeneous tissue models through spheroid fusion within self-healing hydrogels, Nat. Commun. 12 (2021) 753, https://doi.org/10.1038/s41467-021-21029-2.

[43] J.E. Mealy, J.J. Chung, H.-H. Jeong, D. Issadore, D. Lee, P. Atluri, J.A. Burdick, Injectable granular hydrogels with multifunctional properties for biomedical applications, Adv. Mater. 30 (2018) 1705912, https://doi.org/10.1002/adma.201705912.

[44] V.G. Muir, T.H. Qazi, J. Shan, J. Groll, J.A. Burdick, Influence of microgel fabrication technique on granular hydrogel properties, ACS Biomater Sci. Eng. 7 (9) (2021) 4269–4281.

[45] T.H. Qazi, J. Wu, V.G. Muir, S. Weintraub, S.E. Gullbrand, D. Lee, D. Issadore, J.A. Burdick, Anisotropic Rod-Shaped Particles Influence Injectable Granular Hydrogel Properties and Cell Invasion, (2021) 2021.09.23.461542. https://doi.org/10.1101/2021.09.23.461542.

[46] S. Xin, D. Chimene, J.E. Garza, A.K. Gaharwar, D.L. Alge, Clickable PEG hydrogel microspheres as building blocks for 3D bioprinting, Biomater. Sci. 7 (2019) 1179–1187, https://doi.org/10.1039/C8BM01286E.

[47] C.B. Highley, K.H. Song, A.C. Daly, J.A. Burdick, Jammed microgel inks for 3d printing applications, Adv. Sci. 6 (2019) 1801076, https://doi.org/10.1002/advs.201801076.

[48] L. Riley, L. Schirmer, T. Segura, Granular hydrogels: emergent properties of jammed hydrogel microparticles and their applications in tissue repair and regeneration, Curr. Opin. Biotechnol. 60 (2019) 1–8, https://doi.org/10.1016/j.copbio.2018.11.001.

[49] M. Hirsch, A. Charlet, E. Amstad, 3D printing of strong and tough double network granular hydrogels, Adv. Funct. Mater. 31 (2021) 2005929, https://doi.org/10.1002/adfm.202005929.

[50] M. Kessler, T. Yuan, J.M. Kolinski, E. Amstad, Influence of the degree of swelling on the stiffness and toughness of microgel-reinforced hydrogels, Macromol. Rapid Commun. (2023) e2200864.

[51] M. Kessler, Q. Nassisi, E. Amstad, Does the size of microgels influence the toughness of microgel-reinforced hydrogels? Macromol. Rapid Commun. 43 (2022) 2200196, https://doi.org/10.1002/marc.202200196.

[52] R.L. Gustafson, J.A. Lirio, Binding of divalent metal ions by crosslinked polyacrylic acid, J. Phys. Chem. 72 (1968) 1502–1505, https://doi.org/10.1021/j100851a018.

[53] T. Zhang, M.S. Silverstein, Doubly-crosslinked, emulsion-templated hydrogels through reversible metal coordination, Polymer 126 (2017) 386–394, https://doi.org/10.1016/j.polymer.2017.07.044.

[54] J. Fan, S.-H. Kim, Z. Chen, S. Zhou, E. Amstad, T. Lin, D.A. Weitz, Creation of faceted polyhedral microgels from compressed emulsions, Small 13 (2017) 1701256, https://doi.org/10.1002/smll.201701256.

[55] T. Heida, J.W. Neubauer, M. Seuss, N. Hauck, J. Thiele, A. Fery, Mechanically defined microgels by droplet microfluidics, Macromol. Chem. Phys. 218 (2017) 1600418, https://doi.org/10.1002/macp.201600418.

[56] J.M. de Rutte, J. Koh, D. Di Carlo, Scalable high-throughput production of modular microgels for in situ assembly of microporous tissue scaffolds, Adv. Funct. Mater. 29 (25) (2019) 1900071.

[57] L.P.B. Guerzoni, J.C. Rose, D.B. Gehlen, A. Jans, T. Haraszti, M. Wessling, A.J. C. Kuehne, L. De Laporte, Cell encapsulation in soft, anisometric poly(ethylene)

glycol microgels using a novel radical-free microfluidic system, Small 15 (2019) 1900692, https://doi.org/10.1002/smll.201900692.

[58] V. Chimisso, S. Conti, P. Kong, C. Fodor, W.P. Meier, Metal cation responsive anionic microgels: behaviour towards biologically relevant divalent and trivalent ions, Soft Matter 17 (2021) 715–723, https://doi.org/10.1039/D0SM01458C.

[59] M. Steinacher, E. Amstad, Spray-assisted formation of micrometer-sized emulsions, In Review (2021). https://doi.org/10.21203/rs.3.rs-152490/v1.

[60] A. Sinclair, M.B. O'Kelly, T. Bai, H.-C. Hung, P. Jain, S. Jiang, Self-healing zwitterionic microgels as a versatile platform for malleable cell constructs and injectable therapies, Adv. Mater. 30 (2018) 1803087, https://doi.org/10.1002/adma.201803087.

[61] B. Kessel, M. Lee, A. Bonato, Y. Tinguely, E. Tosoratti, M. Zenobi-Wong, 3D bioprinting of macroporous materials based on entangled hydrogel microstrands, Adv. Sci. 7 (2020) 2001419, https://doi.org/10.1002/advs.202001419.

[62] H. Yuk, J. Wu, T.L. Sarrafian, X. Mao, C.E. Varela, E.T. Roche, L.G. Griffiths, C. S. Nabzdyk, X. Zhao, Rapid and coagulation-independent haemostatic sealing by a paste inspired by barnacle glue, Nat. Biomed. Eng. (2021) 1–12, https://doi.org/10.1038/s41551-021-00769-y.

[63] D. Moon, M.-G. Lee, J.-Y. Sun, K.H. Song, J. Doh, Jammed microgel-based inks for 3d printing of complex structures transformable via ph/temperature variations, Macromol. Rapid Commun. 43 (19) (2022) 2200271.

[64] T.H. Qazi, J. Wu, V.G. Muir, S. Weintraub, S.E. Gullbrand, D. Lee, D. Issadore, J. A. Burdick, Anisotropic rod-shaped particles influence injectable granular hydrogel properties and cell invasion, Adv. Mater. 34 (2022) 2109194, https://doi.org/10.1002/adma.202109194.

[65] M.L. Bedell, A.M. Navara, Y. Du, S. Zhang, A.G. Mikos, Polymeric systems for bioprinting, Chem. Rev. 120 (2020) 10744–10792, https://doi.org/10.1021/acs.chemrev.9b00834.

[66] M. Lee, R. Rizzo, F. Surman, M. Zenobi-Wong, Guiding lights: tissue bioprinting using photoactivated materials, Chem. Rev. 120 (2020) 10950–11027, https://doi.org/10.1021/acs.chemrev.0c00077.

[67] Y.S. Zhang, G. Haghiashtiani, T. Hübscher, D.J. Kelly, J.M. Lee, M. Lutolf, M. C. McAlpine, W.Y. Yeong, M. Zenobi-Wong, J. Malda, 3D extrusion bioprinting, Nat. Rev. Methods Primer. 1 (2021) 1–20, https://doi.org/10.1038/s43586-021-00073-8.

[68] J.-Y. Sun, X. Zhao, W.R.K. Illeperuma, O. Chaudhuri, K.H. Oh, D.J. Mooney, J. J. Vlassak, Z. Suo, Highly stretchable and tough hydrogels, Nature 489 (2012) 133–136, https://doi.org/10.1038/nature11409.

[69] J.P. Gong, Y. Katsuyama, T. Kurokawa, Y. Osada, Double-network hydrogels with extremely high mechanical strength, Adv. Mater. 15 (2003) 1155–1158, https://doi.org/10.1002/adma.200304907.

[70] W. Li, X. Liu, Z. Deng, Y. Chen, Q. Yu, W. Tang, T.L. Sun, Y.S. Zhang, K. Yue, Tough bonding, on-demand debonding, and facile rebonding between hydrogels and diverse metal surfaces, Adv. Mater. 31 (2019) 1904732, https://doi.org/10.1002/adma.201904732.

[71] J. Lin, S.Y. Zheng, R. Xiao, J. Yin, Z.L. Wu, Q. Zheng, J. Qian, Constitutive behaviors of tough physical hydrogels with dynamic metal-coordinated bonds, J. Mech. Phys. Solids 139 (2020), 103935, https://doi.org/10.1016/j.jmps.2020.103935.

[72] M. Zhong, Y.-T. Liu, X.-Y. Liu, F.-K. Shi, L.-Q. Zhang, M.-F. Zhu, X.-M. Xie, Dually cross-linked single network poly(acrylic acid) hydrogels with superior mechanical properties and water absorbency, Soft Matter 12 (2016) 5420–5428, https://doi.org/10.1039/C6SM00242K.

[73] S. Anjum, P.M. Gurave, B. Gupta, Calcium ion-induced self-healing pattern of chemically crosslinked poly(acrylic acid) hydrogels, Polym. Int. 67 (2018) 250–257, https://doi.org/10.1002/pi.5517.

[74] L.M. Fuhrer, S. Sun, V. Boyko, M. Kellermeier, H. Cölfen, Tuning the properties of hydrogels made from poly(acrylic acid) and calcium salts, PCCP 22 (2020) 18631–18638, https://doi.org/10.1039/D0CP02649B.

[75] D.J. Schupp, X. Zhang, S. Sun, H. Cölfen, Mineral plastic hydrogels from the cross-linking of polyacrylic acid and alkaline earth or transition metal ions, Chem. Commun. 55 (2019) 4913–4916, https://doi.org/10.1039/C8CC08986H.

[76] A.G. Håti, D.C. Bassett, J.M. Ribe, P. Sikorski, D.A. Weitz, B.T. Stokke, Versatile, cell and chip friendly method to gel alginate in microfluidic devices, Lab Chip 16 (2016) 3718–3727, https://doi.org/10.1039/C6LC00769D.

[77] D.C. Bassett, A.G. Håti, T.B. Melø, B.T. Stokke, P. Sikorski, Competitive ligand exchange of crosslinking ions for ionotropic hydrogel formation, J. Mater. Chem. B 4 (2016) 6175–6182, https://doi.org/10.1039/C6TB01812B.

[78] J.P. Gong, Why are double network hydrogels so tough? Soft Matter 6 (2010) 2583–2590, https://doi.org/10.1039/B924290B.

[79] J.P. Gong, Materials both tough and soft, Science 344 (2014) 161–162, https://doi.org/10.1126/science.1252389.

[80] G.E. Fantner, T. Hassenkam, J.H. Kindt, J.C. Weaver, H. Birkedal, L. Pechenik, J. A. Cutroni, G.A.G. Cidade, G.D. Stucky, D.E. Morse, P.K. Hansma, Sacrificial bonds and hidden length dissipate energy as mineralized fibrils separate during bone fracture, Nat. Mater. 4 (2005) 612–616, https://doi.org/10.1038/nmat1428.